Journal of Manufacturing Processes 131 (2024) 866–878

Contents lists available at ScienceDirect

Journal of Manufacturing Processes

journal homepage: www.elsevier.com/locate/manpro

Thermal-fluid modeling and simulation of Ti-6Al-4V alloy filaments during shaping in the hot-end of material extrusion additive manufacturing

Gaius Chukwuka Nzebuka [a,b], Chukwuzubelu Okenwa Ufodike [a,c,d,*], Al Mazedur Rahman [e], Matthew B. Minus [f], Chijioke Peter Egole [g]

[a] Department of Engineering Technology and Industrial Distribution, Texas A & M University, 3367 TAMU, College Station, TX 77843, United States
[b] Department of Mechatronics Engineering Federal University of Technology, Owerri, Imo State +234, Nigeria
[c] J. Mike Walker'66 Department of Mechanical Engineering, Texas A&M University, College Station, TX 77843, United States
[d] Department of Multidisciplinary Engineering, Texas A&M University, College Station, TX 77843, United States
[e] Department of Industrial & Systems Engineering, Texas A&M University, College Station, TX 77843, United States
[f] Department of Chemistry, Prairie View A&M University, 100 University Drive, Prairie View, TX 77446, United States
[g] Department of Materials and Metallurgical Engineering Federal University of Technology, Owerri, Imo State +234, Nigeria

ARTICLE INFO

Keywords:
Material extrusion
Additive manufacturing
Metal filament
Simulation
Powder

ABSTRACT

Continuous progress in material extrusion additive manufacturing is motivated by the need to produce functional parts at a low cost for medical, aerospace, and automotive applications. A significant innovation is impregnating a polymeric melt with metal powder (particle) to produce a filament that will be 3D printed using a low-cost desktop printer. The presence of metal particles affects the complex flow dynamic and temperature profile during processing through the hot-end of the 3D nozzle. The current study employs numerical simulation to analyze the effect of powder content on the outlet flow field during the melting of polymer-filled metal filament material extrusion additive manufacturing. Titanium 64-5 filament was experimentally measured to obtain thermophysical properties and another Titanium 64-5 filament thermophysical properties were empirically determined. Each filament was simulated using a finite element method to obtain temperature, viscosity, and shear rate data. A detailed discussion of the implementation of the thermal-fluid model was presented. The results obtained indicate that the two types of filaments' sensitivity to the feeding rates differ at a certain region of the extrusion regime. Also, further simulation was performed to investigate the response of the flow fields with the powder contents. The temperature and viscosity results obtained at the nozzle outlet indicate that at a high powder content, the printing of the polymer-filled metal filament can be performed at a high extrusion rate with possible extrudate shape stability. The thermal-fluid model and simulation can be used for selecting process parameters for any new binder-metal particle formulation.

1. Introduction

Functional metal parts used in medical, aerospace, and automotive applications can be made using an additive manufacturing (AM) process. However, AM using direct metal printing, such as selective laser melting, laser powder bed fusion, electron beam melting, and direct energy deposition, generally consumes high amounts of energy, encounters hazards during printing due to handling of the metal powder, has a high production cost, and results in a compromised microstructure of the manufactured part due to localized heating [1–3]. Researchers have reported compromised microstructure of AM printing of metals such as Ti-6Al-4V alloy functional parts using some of the above methods with poor mechanical properties [4–6]. Another major problem in using the above methods of AM for fabricating metal parts is difficulties in removing powder from complex internal structures such as holes after printing [7]. These challenges have motivated an alternative process of manufacturing metals at a low-cost using polymer-filled metal filament (PMF) material extrusion additive manufacturing (AM). The use of PMF in material extrusion AM ensures that metal particles in micro and nano sizes are restricted from being airborne, thereby, promoting safety and cheap technology with less sophisticated machine installation [7]. The PMF is a mixture of a polymer binder system and

* Corresponding author at: Department of Engineering Technology and Industrial Distribution, Texas A & M University, 3367 TAMU, College Station, TX 77843, United States.
E-mail address: ufodike@tamu.edu (C.O. Ufodike).

https://doi.org/10.1016/j.jmapro.2024.09.040
Received 14 April 2024; Received in revised form 12 July 2024; Accepted 12 September 2024
Available online 25 September 2024

metal powder compounded to produce a filament of 1.75 mm or 2.8 mm diameter. The mixture of the binder and metal particles can also be called highly-filled polymers [8]. The PMF material extrusion or metal fused filament fabrication (MF^3) technology comprises three steps; (1) shaping or printing a functional part (green part) with a regular desktop 3D printer, (2) applying solvent and thermal debinding to remove polymer binders, and (3) sintering to densify the parts [8–14].

The focus of the current study is on the first step of MF^3 i.e., the material extrusion of the PMF through the hot-end of a regular desktop 3D printer. The material extrusion is one of the important steps because it determines the shape and stability of the green parts. Gonzalez et al. [9] used a rigorous trial-and-error method to optimize the printing process parameters for the fabrication of the green part. However, the trial-and-error method is a time-consuming and costly process [15]. Hence, the computational approach will significantly reduce the trial-and-error involved in selecting the optimal process parameters, provide more understanding of the complex flow through the hot-end, provide process windows to produce a green part with different concentrations of metal powders, and offer design alternatives in the event of a change in the hot-end design or new materials.

Computational fluid dynamics (CFD) has been used by different researchers in recent years to investigate the flow through the hot-end and predict the process parameters of unfilled or neat polymers [16–23]. Some of these models have been used to predict flow field variables such as viscosity, pressure, temperature, and extrusion force [16–18,20,21,24] of unfilled polymer filament during material extrusion AM through the hot-end. Their findings revealed there is a relationship between the process parameters and the flow variables. However, it is of interest to note that the particle-particle and particle-solvent (fluid) interactions during the melting of PMF will significantly affect the viscosity, shear rate, pressure, extrusion force, velocity, and temperature of the melt which will generate a need for the use of process parameters different from that of neat polymers. As an example, Singh et al. [12] measured the maximum force 59 vol% (87 wt%) Ti-6Al-4V and a neat ABS filament can sustain before failure. Their work revealed that [12] the sustainable force before failure for the ABS filament is 15 times greater than that of the 59 vol% Ti-6Al-4V filament. Additionally, Singh et al. [12] attempted to use the analytical isothermal pressure relations of Hopmann and Michaeli [25] to predict the extrusion force and use the data generated to define limiting feeding rates for printing Ti-6Al-4V filament. However, such analytical models has been reported to underpredict extrusion force due to simplifying assumptions made during derivation [26]. To the best knowledge of current authors, no reported work has been done on the use of the thermal-fluid numerical model to study the combined effect of particle loading and other process parameters to simulate melt flow through the hot-end of a material extrusion AM of any PMF.

The process parameters can be classified into three categories [27]; (1) operation parameters such as extrusion or printing temperature and road width, (2) machine parameters such as nozzle diameter, barrel length, filament feeding rate, and flow rate, and (3) materials parameters such as powder content, binder characteristics, density, specific heat capacity, thermal conductivity, and viscosity. The filament feeding rate is one of the most influential parameters that determines the upper limit for smooth printing of unfilled polymers used in fused filament fabrication (FFF), and there is a relationship between the filament feed rate (F_R), the volumetric flow rate (Q_f), and the printing speed (v_p). The following relationship has been suggested by [23,27];

$$Q_f = \pi r_f^2 F_R \tag{1}$$

$$v_p = \frac{Q_f}{\pi r_e^2} = \frac{r_f^2 F_R}{r_e^2} \tag{2}$$

where r_f and r_e are the filament and extrudate radius respectively. Eqs. (1) and (2) is related to the dimensionless Graetz number (Gz) [28], which can be written in the case of material extrusion AM as follows [21,23].

$$\mathrm{Gz} = \frac{Q_f \rho c_p}{L_b k} = \frac{v_p \pi r_e^2 \rho c_p}{L_b k} = \frac{F_R \pi r_f^2 \rho c_p}{L_b k} \tag{3}$$

where ρ, k, c_p are the density, thermal conductivity, and specific heat capacity of the polymer, and L_b is the barrel length. From Eq. (3), the Gz is a measure of heat transfer by advection to heat transfer by conduction. Therefore, from the machine parameters perspective, increasing either the Q_f, or F_R, or v_p will increase the Gz and favor heat transfer by advection of the polymer in the hot-end. Also, increasing the L_b will decrease the Gz thereby increasing heat transfer by conduction. From the material parameter perspective, increasing the material density and specific heat will increase the Gz thereby hampering the heat transfer while an increase in the thermal conductivity will decrease Gz which will improve heat transfer by conduction [21].

Unfilled polymer filaments generally have low thermal conductivity, low density, and high specific heat capacity when compared to the highly filled metal particle polymer filament. If the machine parameters are kept constant, introducing metal particles in the polymer matrix to produce PMF will increase the density, lower the specific heat capacity, and increase the thermal conductivity of the mixture with a resultant effect on the Gz. Also, varying metal powder content in the mixture will affect other thermophysical properties (such as the viscosity, density, thermal conductivity, etc.) of the system with a subsequent impact on the heat transfer mechanism and other flow variables. Therefore, the process parameters for printing PMF using FFF will be different from the ones used for regular and unfilled polymer filaments. In one related work, Go et al. [29] measured the maximum sustainable force for an unfilled polymer filament and it turned out that the maximum force reported was >60 times greater than that measured in [12] for Ti-6Al-4V filaments. Again, this has emphasized the reason why the relationship between process parameters and flow variables in material extrusion AM of PMF should be investigated. The ongoing discussion is what motivated the current research.

Different PMF commercial manufacturers have reported different powder content compositions in volume and mass percentage for the same metal particle such as the Ti-6Al-4V PMF. The experimental measurement of the thermophysical properties of the PMF for different amounts of metal powder content in the mixture is very costly and time-consuming. Therefore, researchers have adopted empirical and semi-empirical models to predict the thermophysical properties of metal injection molding materials and PMF's feedstocks [11,30,31]. The empirical models have shown very good results when compared to the experimentally measured thermophysical properties of PMF [32].

In this paper, a current important gap in the literature was addressed through the utilization of empirically estimated and experimentally characterized material properties in a CFD model to investigate the effect of some machine and material parameters on the flow of PMF material extrusion additive manufacturing used for the fabrication of functional metal parts from Ti-6Al-4V alloy (or Titanium 64-5). The Titanium 64-5 filament was chosen because Ti-6Al-4V alloy has huge market demand and wide engineering applications such as usage in joint replacement [7]. A Titanium 64-5 filament was obtained from industry and its thermophysical properties were experimentally measured. The measured thermophysical properties of the industrially formulated filament were compared to empirically estimated thermophysical properties of another Titanium 64-5 filament compounded with a different binder system. The data used for the empirical estimation of Titanium 64-5 filament thermophysical properties are obtained from the literature [31,33–35]. The powder contents were varied to identify the effect on the flow characteristics and temperature field in the nozzle which can be useful in identifying the optimum process parameter window during the material extrusion of new PMF. The thermophysical properties of both filaments were used to perform thermal-fluid

simulation, and their respective thermal and flow performance were presented and compared. The simulation aids in comparing the sensitivity of the PMF to process parameters. Also, the study would serve as a cost-effective route for the identification of optimal process parameters to fabricate quality functional parts without the need for an actual printing process.

2. Materials and method

2.1. Experimental characterization of thermophysical properties of Ti-6Al-4V polymer-filled metal filament

A 2.85 mm diameter Titanium 64-5 filament was obtained from the Virtual Foundry (The Virtual Foundry Inc., USA). The thermal and rheological characterization of the Titanium 64-5 filament is conducted as follows.

ASTM E1269 was followed to determine the specific heat Cp of the Titanium 64-5 filament. Aluminium Tzero Hermetic pans with lids were utilized for this purpose. These pans, weighing 48.50 mg, were used to seal the testing samples, which had a mass of 13.80 mg. The temperature range for the test was set from 20 °C to 260 °C, with a heating rate of 20 °C per minute. The upper-temperature limit of 260 °C was chosen based on thermogravimetric analysis (TGA) to prevent sample degradation within the test chamber. The instrument provided a temperature precision of ±0.01 °C and a temperature accuracy of ±0.1 °C.

The Hot Disk Thermal Constants Analyzer (Hot Disk TPS 2500S) was utilized to measure the thermal conductivity and ASTM E1225 was followed correspondingly. For the testing process, a Kapton 5465 sensor with a radius of 3.2 mm was employed. This sensor was inserted into two square-shaped Titanium 64-5 Filament samples that were created using a Carver hot isostatic press instrument. Initially, 2.85 mm Titanium 64-5 Filament was cut into small pieces and then subjected to pressing at a temperature of 150 °C. The pressurization and release were repeated multiple times to ensure the absence of any bubbles within the samples. Square-shaped samples with a thickness of 5.5 mm were obtained, and subsequent polishing with sandpapers was performed to enhance the surface roughness. The samples were securely clamped around the sensor, and various power and time settings were tested to obtain consistent and replicable results. All measurements were conducted at a probing depth of 4 mm, with a power of 40 mW and a measuring time of 20 s. The average data was obtained by performing five repeatable runs.

A rheological test was conducted on feedstock mixtures using a Rosand capillary rheometer RH2000 manufactured by NETZSCH Instruments and ASTM D3845 was followed accordingly. The rheometer consists of two barrels with an inner diameter of 15 mm, each equipped with three temperature control zones. The feedstock material was extruded through different capillaries by two parallel pistons within the barrels. The capillaries used were a long capillary with a 1 mm orifice diameter and a length of 16 mm, and a short capillary with a 1 mm orifice diameter and a nominal length of 0 mm. Two pressure transducers (1500 PSI and 10,000 PSI) were employed to measure the pressure at the entrance of the capillary die. The pressure differences obtained from these transducers were utilized to compensate for losses that occur at the capillary entrance and exit. The geometrical characteristics of the dies, including the entrance angle, reduction ratio, and length-to-diameter (L/D) ratio, remained unchanged throughout the study. Bagley and Rabinovich's corrections were applied. The experiments were conducted at 170, 195 °C, and 220 °C at a shear rate change from 100^{-1} to 4000 s^{-1}.

2.2. Empirical determination of thermophysical properties of Ti-6Al-4V polymer-filled metal filament

The material property empirical models presented in Table 1 are those suggested in [11,31], and they have shown good suitability for PMF material extrusion simulation. As reported in [31], the binder consists of paraffin wax, low-density polyethylene, polypropylene, and stearic acid. The details of the description of Eqs. (1)–(7) in Table 1 can be found in [11,31].

The shear viscosity $\eta_b(\dot{\gamma}, T)$ of the binder is sensitive to shear rate and temperature, therefore, it is expressed using the Cross and Arrhenius's relation given as follows.

$$\eta_b(\dot{\gamma}, T) = f(T)\eta(\dot{\gamma}) \tag{8}$$

where

$$f(T) = exp\left[\frac{E_a}{R}\left(\frac{1}{T} - \frac{1}{T_{ref}}\right)\right] \tag{9}$$

$$\eta(\dot{\gamma}) = \frac{\eta_o}{1 + (\lambda\dot{\gamma})^{1-n}} \tag{10}$$

From Eq. (7) in Table 1, the following equation is written for the viscosity of the polymer-filled metal filament.

$$\eta_f(\phi) = \eta_r * exp\left[\frac{E_a}{R}\left(\frac{1}{T} - \frac{1}{T_{ref}}\right)\right] * \frac{\eta_o}{1 + (\lambda\dot{\gamma})^{1-n}} \tag{11}$$

where η_o is the zero shear-rate viscosity, η is the shear viscosity, n is the Power-law index, λ is a time constant, E_a is the activation energy, R is the gas constant, T_{ref} is the reference temperature, T is the temperature, and $\dot{\gamma}$ is the shear rate.

Table 1
Material properties models used to predict thermophysical properties of the PMF [11,31].

Material property	Model	Equation number	Variable definitions
Density	$\rho_f = \frac{\rho_p\rho_b}{M_b\rho_p + M_p\rho_b}$ where $M_p = \frac{\phi_p\rho_p}{\phi_p\rho_p + \phi_b\rho_b}$ $M_b = \frac{\phi_b\rho_b}{\phi_p\rho_p + \phi_b\rho_b}$ $\phi_p = \frac{\frac{M_p}{\rho_p}}{\frac{M_p}{\rho_p} + \frac{M_b}{\rho_b}}$ $\phi_b = 1 - \phi_p$	(4)	ρ, M, and ϕ are the density, mass fraction, and the volume fraction, respectively.
Specific heat	$C_{pf} = (C_{pp}M_p + C_{pb}M_b) * (1 + 0.2 * M_pM_b)$	(5)	C_p is the specific heat capacity at constant pressure.
Thermal Conductivity	$1 - \phi_p = \left(\frac{k_p - k_f}{k_p - k_b}\right)\left(\frac{k_b}{k_f}\right)^{1/3}$	(6)	K is the thermal conductivity
Viscosity	$\eta_f(\phi) = \eta_r\eta_b(\dot{\gamma}, T)$ where $\eta_r = \frac{1}{\left(1 - \frac{\phi_p}{0.64}\right)^2}$	(7)	η is the viscosity.

The subscript *f, p b,* and *r* stand for the feedstock, powder, binder, and relative, respectively.

2.3. Modeling and simulation of the polymer-filled metal filament

Fig. 1 provides the hot-end with different views and the simulation domain. The filament enters through the upper cylindrical section of the heat sink at specified feeding rates into the cylindrical barrel section of the heater block where it is heated up and traveled through a conical-capillary section where the filament is assumed to be fully melted depending on the temperature and feeding rates before exiting for printing. The geometrical information of the nozzle is similar to the one used in the previous publication [17] which is the same as the E3D nozzle. Due to the symmetry of the computational domain only half of the geometry is modeled. Hence, the flow of the polymer is assumed to be 2D-axisymmetric cylindrical coordinates. Further assumptions used in the development of the governing equations are that the binder system and the particles are modeled as a continuous region, therefore, a continuum model was assumed to formulate the generalized Newtonian flow. Also, the flow is incompressible, transient, laminar, constant thermal conductivity, and viscous dissipation are considered. The governing equations are presented as follows [36–38].

$$\nabla.\boldsymbol{u} = 0 \tag{12}$$

$$\rho\frac{Du}{\partial t} = -\nabla P + \nabla.\left(2\eta_f(\phi)D\right) \tag{13}$$

$$\rho c_p\frac{DT}{\partial t} = -\nabla(k\nabla T) + \sigma:\dot{\gamma} \tag{14}$$

where

$$D = \frac{1}{2}\left(\nabla\boldsymbol{u} + \nabla\boldsymbol{u}^T\right) \tag{15}$$

$$\dot{\gamma} = \sqrt{2tr(D)^2} \tag{16}$$

σ is the Cauchy stress tensor, and D is the rate of deformation tensor, therefore the term $\sigma:\dot{\gamma}$ represents the viscous dissipation for non-Newtonian fluid.

The following boundary conditions are used to solve Eqs. (12)–(16). At the inlet, a constant prescribed velocity and temperature are imposed. The inlet velocity is equivalent to the feeding rate and the inlet temperature is taken at ambient conditions. A slip boundary condition was imposed on the barrel wall. The reason for the flow slip boundary condition is justified by noting that the slip is a dominant physical phenomenon than shear stresses at the walls for highly-filled polymers [39–42], therefore viscous forces and hydrodynamic boundary layer development are negligible at the barrel wall. The thermal boundary conditions at the barrel wall were defined by recognizing that the barrel diameter (3.2 mm) is larger than the filament diameter (2.85 mm), so there is a small airgap between the solid filament and the barrel wall, therefore, the heat flux per unit area is used as presented in the following relation.

$$q = h(T_l - T_s) \tag{17}$$

where T_l and T_s are the liquefier wall and filament surface temperatures, respectively, h is the convective heat transfer coefficient. The convective heat transfer coefficient used in the simulation was determined using a technique suggested in [17]. The method includes the use of dynamic and geometrical similarity of the Nusselt number *Nu*. A heat transfer coefficient was calibrated from experimentally determined force data, from which the Nusselt number was also obtained. Then the heat transfer coefficient h_c of the current simulation is determined using the following relation.

$$Nu_e = Nu_c = \frac{h_e 2r_1}{k_1} = \frac{h_c 2r_2}{k_2} \tag{18}$$

where h_e and h_c are the experimentally calibrated and the calculated heat transfer coefficients, respectively, k_1 and k_2 are the thermal conductivities of material where the h_e was calibrated from and the current material(s) under investigation, respectively, $2r_1$ is the diameter of the filament where h_e was calibrated from and $2r_2$ is the current simulation filament diameter, and the subscripts e and c represent experimentally calibrated and calculated. The h_e value used in the estimation of h_c is 215 W/m^{2}K [16]. This value was used because it was obtained by calibrating the heat transfer coefficient through the adjustment and iteration of the convective heat transfer coefficient to obtain a value that predicted the experimentally measured feeding force more accurately. The method of calibrating the convective heat transfer coefficient from experimental data was also adopted in [17,20,21].

For the converging section of the nozzle, it has been observed that the shear rate is significantly accompanied by high shear stresses [17,18,20,21,24], therefore, shear-induced flow significantly dominates the wall slip flow [39]. Therefore, no-slip boundary conditions were imposed on the conical and capillary walls. For the thermal boundary, specified constant temperatures were imposed at the conical and capillary walls. An outflow and symmetry boundary conditions were imposed at the outlet and symmetry axis, respectively for all flow variables.

2.3.1. Numerical solution method

The governing equations were implemented in a finite element commercial software ANSYS Polyflow and the software has an inbuilt program that solves Eqs. (12)–(16) [43]. A mesh convergence test was performed to determine an optimal computational mesh of 34,483 elements which was selected based on accuracy and computational cost and it ensured that the solution was independent of the mesh size. The

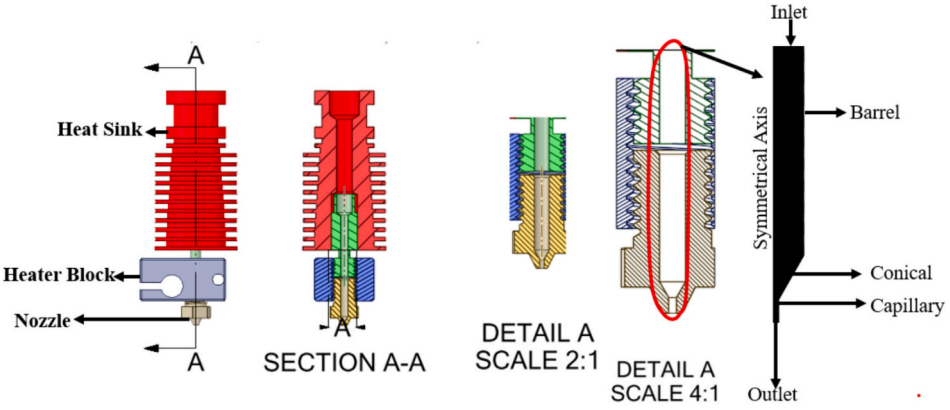

Fig. 1. Illustration of the hot-end showing sectional and detailed views of the physical and simulation domain under study. Dimensions [17]: inlet; 3.2 mm, Barrel; 17.6 mm, Conical angle; 30°, Capillary; 1.2 mm, Outlet; 0.6 mm.

finite element method utilizes a combined interpolation method to discretize and solve the pressure-velocity coupling. The velocity and pressure fields were represented by quadratic and linear continuous interpolations, respectively. In the energy equation, a combination of quadratic elements for temperature and upwinding was used. To tackle the nonlinearities and numerical stiffness that arise in the computation of shear-rate-temperature dependent viscosity, the Picard iteration scheme was used since it provides better solution convergence for the power-law index n <0.7. In the transient scheme, the Crack-Nicolson second-order time marching was used with automatic time stepping. To ensure numerical solution stability and reduction in the computational time, the minimum and maximum time steps were set to 0.001 and 0.8, respectively, with a tolerance time marching value of 0.01. The maximum number of iterations for each time step is 40. Due to the nonlinearities arising during the calculation of the generalized Newtonian flows with shear-rate-temperature dependent viscosity and slip boundary condition, a steady-state calculation was first obtained by enabling convergence strategies in rheology/slip, thermal flows, and decoupled computation of velocity and temperature. Then the converged steady-state solution result was exported to a comma-separated values (CSV) file that contains both the coordinates and all the flow variable data. The CSV file was imported was used as an initial condition for the transient calculation. In the transient calculation, the velocity and temperature were coupled, and the solution was solved until convergence was achieved at every time step.

3. Results and discussion

3.1. Comparison of the thermophysical properties of the experimentally characterized and empirically estimated polymer-filled metal filament

For brevity, the feedstock properties obtained using experimental characterization is labeled EXP feedstock or simply EXP, and that estimated using the empirical model is labeled EMP feedstock or simply EMP. The thermophysical properties of the EMP were obtained using the known binder system and Ti-6Al-4V alloy properties presented in [31,33–35]. The industry technical and safety data sheet information of the EXP feedstocks revealed that the binder (solvent) system is majorly polylactic acid. The quoted mass percentage of Ti-6Al-4V particles in the solvent is 80 wt%, and the density is 2460 kg/m^3. Based on the 80 wt% and taking the density of the PLA binder and Ti-6Al-4V alloy to be 1220 kg/m^3 as given in [17] and 4420 kg/m^3 as given in [31], respectively, using Eq. (4), the theoretically estimated Virtual Foundry binder density is 886.88 kg/m^3, and the estimated volume percentage of Ti-6Al-4V particle in the binder system is 44.5 vol%. The empirical models presented in Table 1 were used to predict the thermophysical properties of EMP feedstock. The Ti-6Al-4V particle content in the binder used in the current section is 44.5 vol% which was selected to correspond to EXP particle content. Using the binder density of 880 kg/m^3 as given in [31], and the Ti-6Al-4V alloy density, the estimated EMP feedstock density is 2456 kg/m^3. This indicates that both the values of the binder density and feedstock density for EXP and EMP are similar with minor differences as summarised in Table 2 below.

Table 3 is the rheological fitted data for EXP and EMP feedstock. The table shows that the power law index is <0.7 which justifies why the Picard iteration scheme was selected in the simulation as stated in the previous section. The specific heat capacity of EXP is presented in Fig. 2 showing an abrupt change in the slope at 342 K which corresponds to the glass transition temperature.

Table 2
Material density comparison at 44.5 vol%.

Feedstock	Binder density kg/m^3	Feedstock density kg/m^3
EXP	886 (predicted)	2460 (Industry)
EMP	880 (measured, [31])	2456 (Predicted)

Table 3
Rheological data of the two filaments at 44.5 vol%.

Cross model constants	EXP	EMP
η_o (Pa·s)	3398	3077
$\frac{E_a}{R}$ (K)	10,142	16,400
n	0.25	0.39
λ (s)	0.12	0.18
T_{ref} (K)	468	413

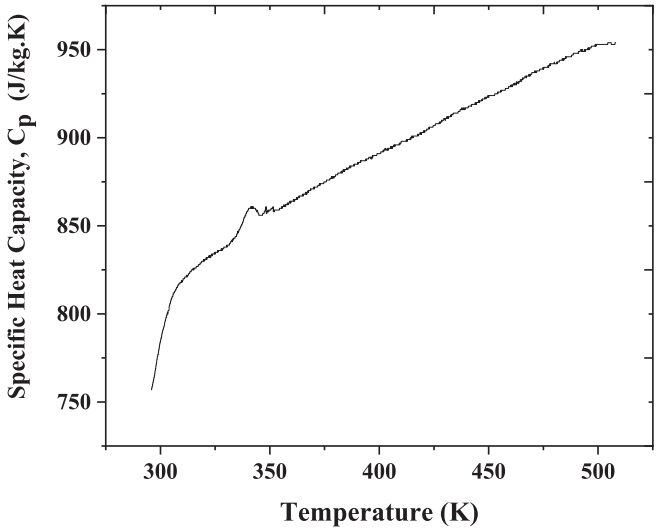

Fig. 2. Specific heat capacity versus temperature of EXP filaments.

Table 4 presents the specific heat capacities C_{pf} of EXP and EMP. The temperature of the specific heat capacity data for EXP was carefully selected to correspond to the temperature at which the values of the C_{pf} for EMP were predicted, thus allowing for comparison and analysis. The selected temperature points correspond to the experimentally determined specific heat capacity of the EMP binder. The table indicates that the specific heat capacities of the two feedstocks vary significantly from each other. The main reason for this variation may be attributed to the binder components and additives used to formulate the two feedstocks. A drop in the value of the of the C_{pf} beyond 331 K is evident in Table 4 for EMP feedstock which is a trend that is posited to be transmitted from the experimentally measured values of the binder-specific heat capacity. Also, the specific heat capacity of EMP feedstock is highly non-linear. For instance, from 303 K the C_{pf} of EMP increases with temperature until 331 K, then decreases below the value predicted for the lowest temperature and increases slightly at the highest temperature.

The same trend was observed in the measured specific heat capacity of the binder as reported in [31]. For the EXP feedstocks, the C_{pf} increases with temperature, with the lowest value recorded at the lowest temperature and the highest value recorded at the highest temperature as shown in Table 4.

To calculate the thermal conductivity of the EMP using Eq. (6), the

Table 4
The empirically and experimentally determined specific capacities at 44.5 vol%.

Temperature (K)	EMP (J/kg·K)	EXP (J/kg·K)
303	1119	800
305	1193	809
322	1223	832
331	1391	839
384	961	882
443	1007	919

Newton-Raphson numerical method was used. Therefore, a MATLAB code was written to iterative solve Eq. (6) until the solution converged. The thermal conductivity values experimentally determined for EXP and empirically predicted for EMP feedstock weakly depend on temperature, therefore, an average value of 0.74 W/m-K and 0.78 W/m-K, respectively, were used for the simulation. It turns out that the two thermal conductivities are almost the same with EMP slightly higher than EXP. The printer's set temperature was 503 K, the nozzle diameter was 0.6 mm, and other dimensions of the hot-end correspond to that used in our previous work [17].

3.2. Simulation results analysis

3.2.1. Thermal comparison of the two polymer-filled metal filaments at the nozzle outlet

In this section, CFD was used to predict the temperature and viscosity of the EXP and EMP. For simulation purposes, two cases of C_{pf} were firstly utilized to inform the final C_{pf} that will be used. First, an average constant value of the C_{pf} presented in Table 4 was evaluated and used for simulation, secondly, the C_{pf} data for EXP and EMP were fitted to obtain a temperature-dependent relation. For the EXP, a polynomial relation of the second order was obtained from Fig. 2 over the entire measured temperature range, while, for EMP the data in the Table 4 was plotted and only the linear portion of the curve that gave the best fit was used. The purpose of using the two approaches stated previously is to obtain a simulation result for EMP C_{pf} that best follows the EXP C_{pf}. For the first case, an average value of 846.83 J/kg·K and 1148.987 J/kg·K were determined for EXP and EMP respectively. For the second case, the following relations were obtained.

$$\text{For EXP of 44.5 vol\%; } C_p(T) = 333.63 + 2.077T - 0.00169T^2 \text{ (J/kg·K)} \quad (19)$$

$$\text{For EMP of 44.5 vol\%; } C_p(T) = 2482.39 - 3.31T \text{ (J/kg·K)} \quad (20)$$

Fig. 3 shows the average temperature at the nozzle outlet against the feeding rate for the constant and temperature-dependent C_{pf} used. The EXP and EMP curves represent temperature-dependents C_{pf} for the first case, while for the second case, EXP_C and EMP_C curves represent the average constants C_{pf}. Below the feeding rate of 60 mm/min, the outlet average temperature of the four cases is almost the same. As the feeding rate increases, the EXP_C curve increases slightly above the EXP curve but with a closer trend in the monotonic drop in temperature. The EMP curve matches closely with the EXP curve than with the EXP_C curve up to a feeding rate of 140 mm/min, then, crosses higher and turns horizontally with an almost constant slope at a higher feeding rate. The EMP_C follows the same trend as the EMP but with a lower temperature of 140 mm/min before turning horizontally with an increase in feeding rate. This indicates that there is a feeding rate (140 mm/min) where an increase in the feeding rate has less or no effect on the average exit temperature of the EMP and EMP_C curve. Further analysis of the simulation results may be required to hypothesize the reason for the sharp deviation in the temperature-feeding rate curve of EMPs and EXPs.

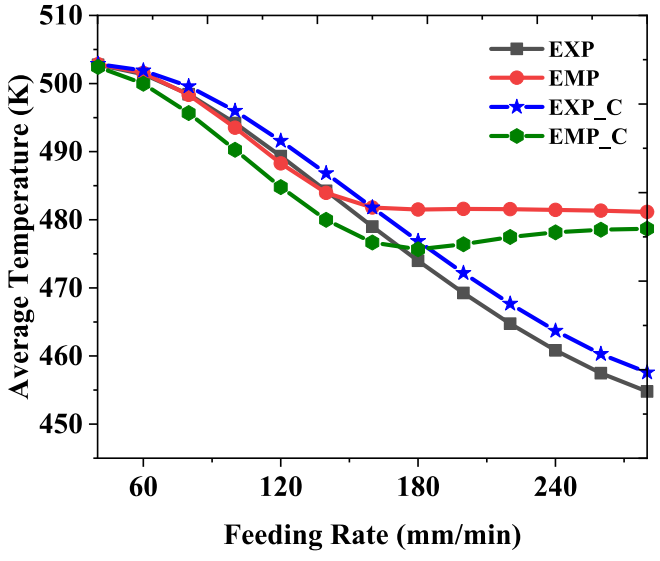

Fig. 3. Average temperature at the nozzle outlet as a function of the feeding rates at a printer set temperature of 503 K and nozzle diameter of 0.6 mm.

Meanwhile, one thing that is deduced in the ongoing discussion is that the EMP curve follows the EXP curve more closely than the EMP_C curve at a feeding rate $\leq$ 140 mm/min. Therefore, subsequent simulations were performed for temperature dependents EXP and EMP C_{pf}.

3.2.2. Spatial variation of the temperature in the converging section of the hot-end

The outcome of the temperature field downstream of the converging (or conical-capillary) section of the hot-end towards the nozzle outlet determines the final extrudate temperature. As noted from the immediate previous section, a divergence in the temperature curve was predicted between EXP and EMP at a feeding rate >140 mm/min. Further analysis of the entire temperature field in the conical-capillary section will deepen understanding of the thermal development. Fig. 4 is the temperature contour of the conical section of the hot-end with a color legend to aid in the.

description of the temperature distribution. The red color highlights the region with the highest temperature of 503 K which corresponds to the conical and capillary inner-wall surface temperature. In Fig. 4a (case with 120 mm/min) the radial growth of the red color towards the central section is larger than in Fig. 4b (case with 180 mm/min). For this study, this region (red-colored) will be identified as a thermal boundary layer. Therefore, the thermal boundary layer zone in Fig. 4a for the EXP at the conical and capillary sections is larger than that of EMP. Also, for Fig. 4b the thermal boundary layer for the EXP is larger than that of the EMP in the conical section, while that of EMP is larger than that of the EXP in the capillary section. To quantify this observed thermal evolution phenomena in the conical and capillary sections, temperature as a function of the radial distance is plotted as depicted in Figs. 5 and 6. Two feeding rates of 120 mm/min and 180 mm/min were selected to correspond to the region where the EMP curve matches closely with EXP curve and where EMP curve turns horizontal with an increase in the feeding rates as depicted previously in Fig. 3.

Figs. 5 and 6 show that the temperature rises from the center to the periphery and the respective temperature curves widen at the center and tend to merge towards the periphery, which is an indication of heat transfer from the wall to the center. Such a trend has also been observed in the hot-end of material extrusion AM for neat polymers as reported elsewhere [16,17,21,24,29]. Fig. 5a shows that at the central axis in the conical section where y = 2.4 mm, the predicted temperature for EXP (461 K) is higher than the temperature for EMP (446 K) which depicts a temperature difference of 15 K. Similarly, in Fig. 5b, the temperature for EXP (428 K) is higher than that of EMP (400 K) with a temperature difference of 28 K.

As the melted polymer-filled metal filament feedstock flows downstream towards the outlet of the capillary section with a feeding rate of 120 mm/min, the difference between the central temperature narrows as depicted in Fig. 6a with EXP curve slightly move above the EMP curve with a temperature difference of 2 K. However, at a feeding rate of 180 mm/min, the predicted temperature for EXP is lower than that of EMP with a difference of 10 K. This again reflects the increase in the boundary layer at a feeding rate of 180 mm/min for EMP as discussed previously in Fig. 4b. This phenomenon correlates very well with the observed monotonic dropped in the average nozzle outlet temperature of EXP as

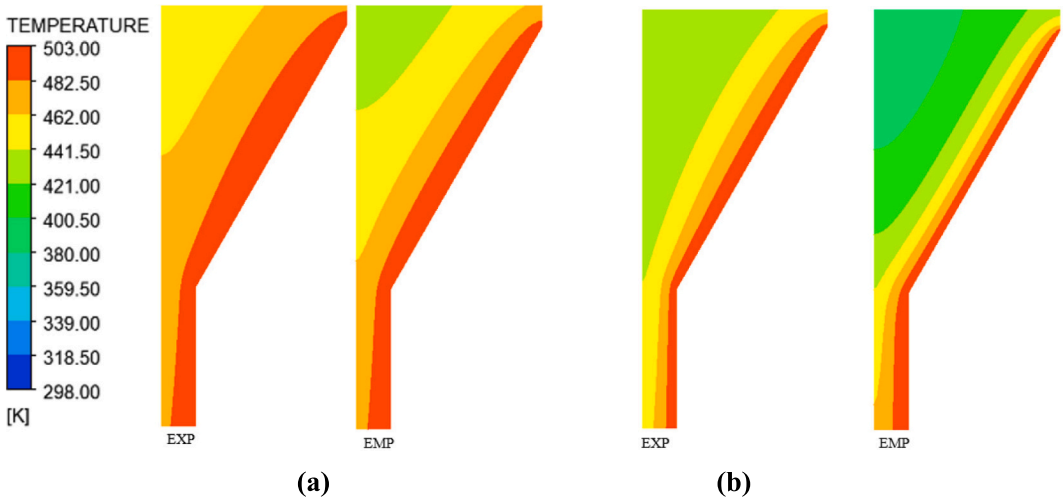

Fig. 4. Temperature distribution at the conical-capillary section at a printer set temperature of 503 K, nozzle diameter of 0.6 mm, (a) 120 mm/min, and (b) 180 mm/min.

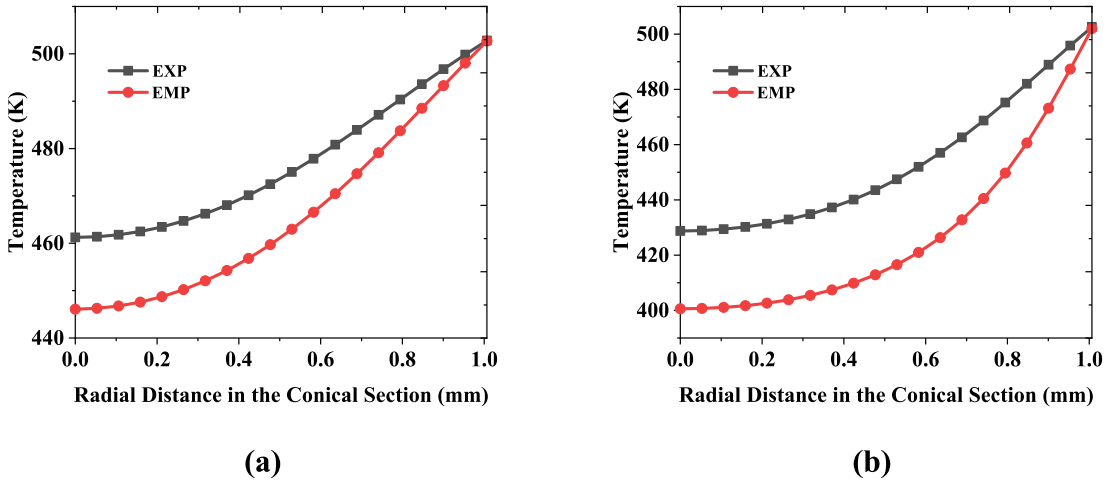

Fig. 5. Temperature as a function of radial distance at the conical section (y = 2.4 mm) (a) 120 mm/min (b) 180 mm/min for a printer temperature of 503 K and 0.6 mm nozzle diameter.

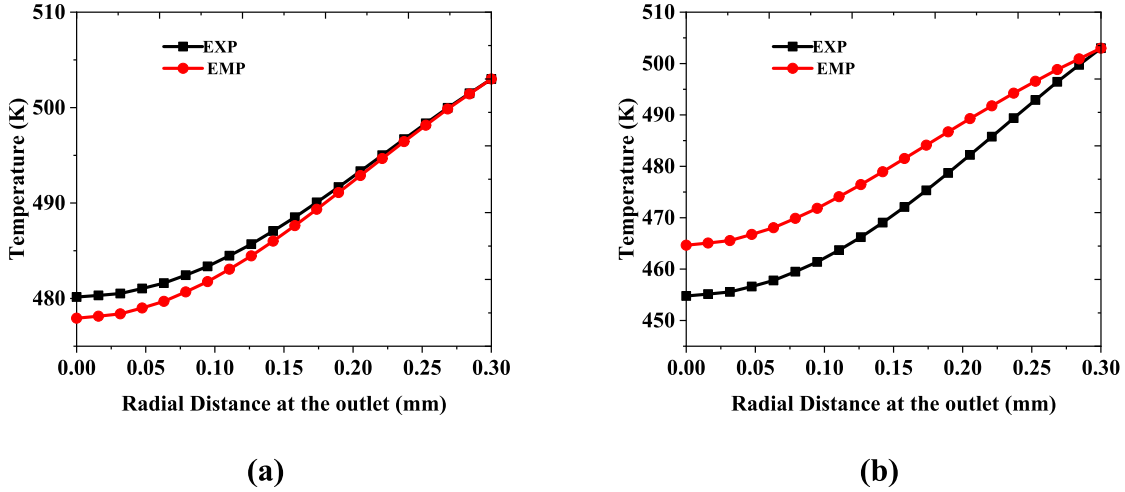

Fig. 6. Temperature as a function of radial distance at the nozzle outlet (a) 120 mm/min (b) 180 mm/min for a printer temperature of 503 K and 0.6 mm nozzle diameter.

the feeding rate increases, with the EMP unaffected with an increase in the feeding rate above 140 mm/min as reported previously in Fig. 3.

To explain the physics behind this phenomenon, it is necessary to note that it occurs at a certain higher feeding rate, above 140 mm/min (as indicated in Fig. 3), and at a narrow flow passage of the capillary nozzle, therefore this must be associated to the sensitivity of the EMP binder-powder particles constituent with the shear rate at higher temperature. Fig. 7 shows the average shear rate and the shear viscosity as a function of the feeding rate and that both the shear rate and viscosity increase as the feeding rate increases. It is obvious from Fig. 7a that the shear rates for the EXP and EMP are almost the same with slight variation beyond the 140 mm/min feeding rate. Above 140 mm/min, the EXP increases slightly more than the EMP as the feeding rate increases.

However, Fig. 7b shows a wider variation in the shear viscosity with the EMP significantly lower than the EXP. The blue arrows from the rectangular shaded region in the abscissa-axis of Fig. 7b point to the zoomed portion of the EMP insert. The lowest predicted average shear viscosity at the lowest feeding rate for EXP and EMP are 238 Pas and 0.7 Pas, respectively. The highest predicted average shear viscosity at the highest feeding rate for EXP and EMP are 12,726 Pas and 12 Pas, respectively.

The comparison of the shear viscosity for both feedstocks (Fig. 7b), shows that the EMP feedstocks may present successive layer-by-layer shape deposition stability difficulties of the green parts since it shows an excessively lower viscosity at all feeding rates investigated. One reported reason for this may be that at a higher temperature, with an increase in the shear rate due to flow restriction at the capillary section of the nozzle, there is a binder separation and breakdown for the EMP feedstock [31]. Another reason may be attributed to the binder components and additives used during EMP feedstock formulation. Further, the amount of paraffin wax which is a low molecular weight polymer and stearic acid in the EMP feedstock can lower the viscosity of the melt. Other factors that could lower the viscosity of polymer-filled metal particles are adherence of the binder to the powder, particle shape, and particle size distribution [11]. Therefore, the observed shear viscosity variation between the EMP and EXP feedstocks can be attributed to the different in binder composition, particle sizes and distribution in each of the feedstocks which informs the sensitivity of the melt to shear rate and temperature.

The ongoing results analysis indicates that, given the same powder loading of 44.5 vol%, the responses of the two feedstocks quantified in terms of shear rate, shear viscosity, and temperature with feeding rates are almost the same at a certain range of extrusion regimes. However, with a further increase in the feeding rate (above 140 mm/min), the responses of the two feedstocks differ greatly with temperature and shear viscosity, slightly with shear rate, and slightly with the outlet velocity (See Fig. 8).

It should be noted that the outlet velocity can be used as a good first estimation of the likely printing speed for printing trials. Hence, Fig. 8 indicates that the outlet velocity is almost the same for both feedstocks with the EMP feedstock having a higher outlet velocity than the EXP as the feeding rates increase. The slightly higher predicted outlet velocity for the EMP is linked to the higher temperatures predicted in Fig. 3.

3.3. Combine effect of feeding rates and metal particle contents on the thermal response of polymer-filled metal filaments

The low viscosity predicted and the observed temperature response for the EMP feedstock with an increase in the feeding rate may also be affected by particle loading, thus, requiring further analysis. In this section, 45, 50, 56, and 60 vol% of powder loading for the EMP metal feedstocks were chosen for the simulation and analysis. The viscosity was calculated using Eq. (7) and data obtained was fitted using Eq. (11) which is Cross and Arrhenius's relation for the shear rate-temperature-dependent viscosity. The density was calculated, the temperature-dependent specific heat capacity was estimated, and the data was also fitted. All the thermophysical properties were predicted using the Eqs. (4)–(7). The thermophysical properties of the binder and the Ti-6Al-4V

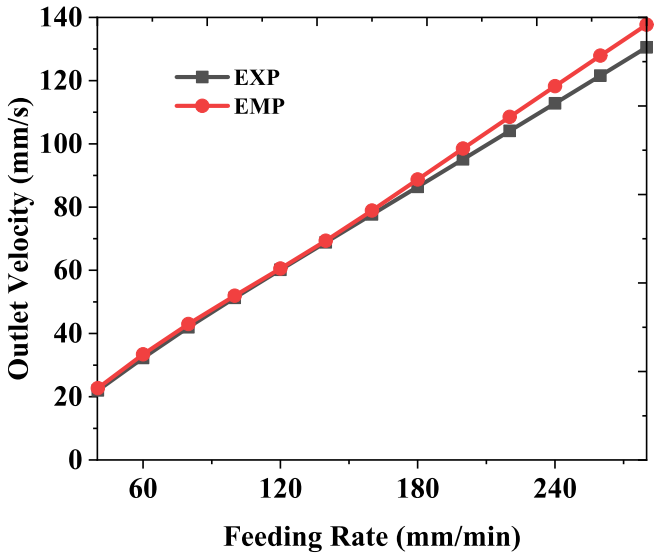

Fig. 8. Outlet velocity as a function of feeding rates at the nozzle outlet for a printer temperature of 503 K and 0.6 mm nozzle diameter.

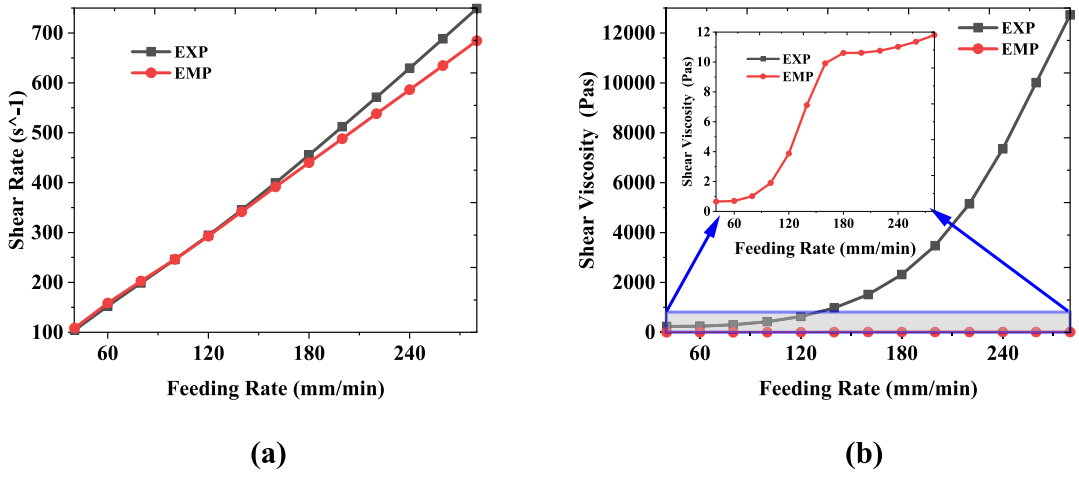

Fig. 7. (a) Shear Rate and (b) Shear Viscosity as a function of feeding rates at the nozzle outlet for a printer temperature of 503 K and nozzle diameter of 0.6 mm.

metal particles used were those presented in [31,33–35]. Tables 5–6 presents the thermophysical properties of the feedstocks. Table 7 shows the fitted rheological properties for the simulation.

Table 6 shows the variation of the thermal conductivities and densities with powder contents which shows that as the powder contents increase the thermal conductivity increases. The thermal conductivity was estimated using the MATLAB code as stated in the previous section and its average values were used due to weak temperature dependence.

For the specific heat capacity, temperature-dependent expressions as stated below were used.

$$\text{For 45 vol\%; } C_p(T) = 2482.37 - 3.29T \text{ (J/kg·K)} \quad (21)$$

$$\text{For 50 vol\%; } C_p(T) = 2184.14 - 2.79T \text{ (J/kg·K)} \quad (22)$$

$$\text{For 56 vol\%; } C_p(T) = 1888.39 - 2.29T \text{ (J/kg·K)} \quad (23)$$

$$\text{For 60 vol\%; } C_p(T) = 1690 - 1.944T \text{ (J/kg·K)} \quad (24)$$

Fig. 9 presents the temperature contour for different powder content of the entire hot-end of metal material extrusion additive manufacturing. The color legend helps to identify regions of cold (blue) representing the upper barrel inlet section and hot (red) regions representing the conical and capillary outlet sections. The blue color-covered region in the upper barrel inlet section moves (decreases) upward and the red color region downstream of the conical capillary moves (increases) upward as the powder content increases from 45 to 60 vol% which indicates a high rate of heat transfer. Also, the spatial distribution of the temperature shows that heat transfer is from the wall to the center of the hot-end.

The reason for an enhanced heat transfer is due to an increase in the thermal conductivity of the feedstock with an increase in metal powder content which indicates that the outlet temperature will be higher at higher powder contents as will be shown in the next discussion.

Fig. 10 shows the average outlet temperature of the feedstock at the nozzle exit and core temperature as a function of the feeding rate for different powder content. The figure shows that as the feeding rate increases the outlet temperature decreases. It should be recalled from Eqs. (1)–(3) that the printing speed increases as the feeding rate increases and the Gz also increases as shown in Fig. 11. The figure (Fig. 11) further shows that the Gz decreases with an increase in the powder contents since the curve for the EMP-60 is lowest. This indicates that the heat transfer by conduction increases and dominates the advective counterpart with an increase in the powder content and vice versa. This is not surprising because the activities of the particle-particle interaction increase the thermal conductivity of the feedstock with an increase in the powder content which in turn decreases the Gz value at any given feeding rate. Therefore, the exit temperature decreases with feeding rates, increases with a decrease in the Gz, and increases with the powder contents and vice versa. For instance, the EMP-45 curve indicates the highest Gz of approximately 8 at the maximum feeding rate of 280 mm/min considered in the current simulation, and this shows that the Gz may tend to increase further with a decrease in particle loading and for an unfilled polymer it is expected to be higher. The estimated Gz of ABS using thermophysical properties provided in [21] at room temperature and the feeding rate of 280 mm/min is 12, which means that the predicted exit temperature should be lower compared to the PMF feedstocks.

The decrease of the nozzle exit temperature with Gz has been recently reported in [23] for a neat (unfilled) polymer feedstock. Additionally, further observation of Fig. 10 indicates at powder content of 45 and 50 vol%, the temperature curves turn horizontally (compare with Fig. 3) and equilibrate as the feeding rate increases. This phenomenon has been reported previously, indicating that there is a threshold powder content in the binder below which temperature drop hesitate with an increase in the feeding rates. However, above 56 vol% of powder contents in the binder, the temperature drop hesitation with feeding rates is less pronounced and a continuous drop in the temperature was evident at powder content of 60 vol%.

Based on the simulation conditions and the limiting assumption considered, it can be hypothesized that at a high powder content, the printing of metal filament can be performed at a high volumetric flow rate (and high printing speed) with a consequence increase in the production of the functional parts.

Fig. 12 is plotted to further illustrate the relationship between the feeding rates, powder contents, outlet velocity (or printing speed), and viscosity. An average value of the velocity and the shear viscosity is plotted in Fig. 12a and b, respectively. The outlet velocity at the nozzle exit is taken to be equivalent to the printing speed if there is no skipping of the stepper motor during extrusion.

The figure reveals that the outlet velocity increases with the feeding

Table 5
Density.

Powder contents	45 vol%	50 vol%	56 vol%	60 vol%
Density, kg/m^3	2473	2650	2862	3004

Table 6
Thermal conductivity.

Powder contents	45 vol%	50 vol%	56 vol%	60 vol%
Thermal conductivity, W/m·K	0.802	0.982	1.263	1.498

Table 7
Rheological-fitted data used for the simulation.

Cross model constants	45 vol%	50 vol%	56 vol%	60 vol%
η_o (Pa·s)	3300	6080	20,136	76,800
$\frac{E_a}{R}$ (K)	16,400	16,400	17,200	17,030
n	0.39	0.39	0.4	0.4
λ (s)	0.18	0.18	0.22	0.19
T_{ref} (K)	413	413	413	413

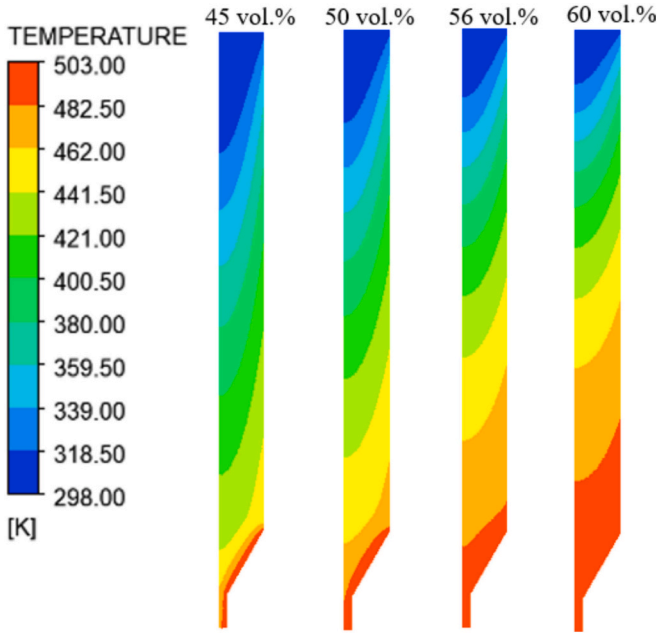

Fig. 9. The temperature distribution through the hot-end during material extrusion of metal additive manufacturing. Simulation condition: feeding rate 0.002 m/s (120 mm/min), printer set temperature of 503 K, and nozzle diameter of 0.6 mm.

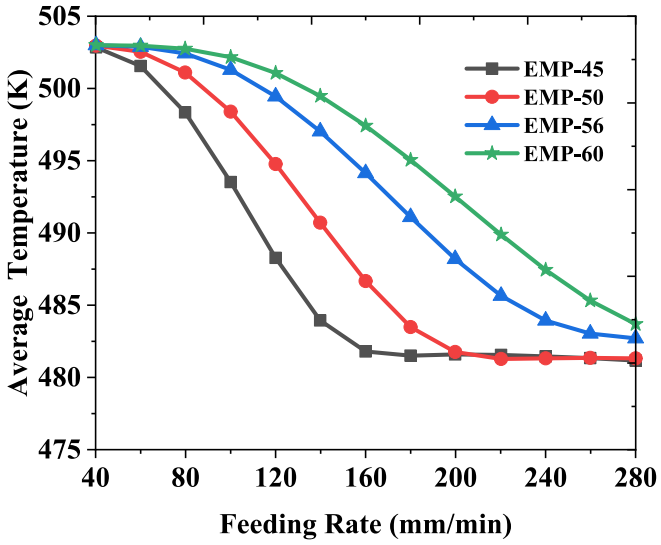

Fig. 10. Average temperature at the nozzle exits as a function of feeding rates for different metal powder content. Simulation condition: printer set temperature of 503 K and nozzle diameter of 0.6 mm.

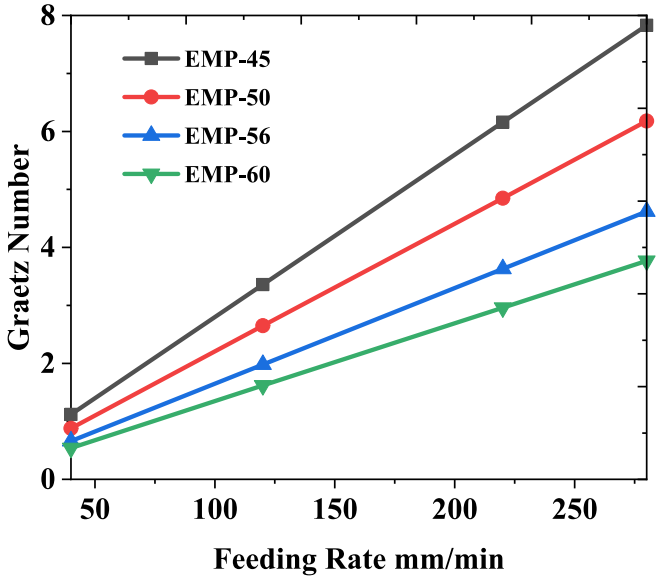

Fig. 11. The Graetz number as a function of the feeding rate for different metal powder content. Estimated at a room temperature of 298 K and liquefier inlet with filament diameter of 2. 85 mm, and barrel length of 17.6 mm.

rate for all the metal powder contents considered. Also, the outlet velocity for the four powder contents considered is almost the same at lower feeding rates (below 80 mm/min) and above 240 mm/min. However, in between the stated feeding rates, the outlet velocity increases slightly as powder contents increase. Quantified results indicate that the outlet velocity at a feeding rate of 140 mm/min the predicted outlet velocity for 45, 50, 56, and 60 vol% are 69, 71, 74, and 76 mm/s, respectively. Note that the inlet and outlet diameter of the physical domain for all the simulations considered are the same which ordinarily should give the same outlet velocity based on continuity, however, the reason for this increase in the outlet velocity may be associated with different factors, but one noticeable factor is associated with the thermal-fluid coupling between the temperature and velocity via the constitutive viscosity model and governing equations. At higher particle loading the thermal conductivity increases due to high interactions between the binder and the metal particles, thus, resulting in high outlet temperature (seen in Fig. 10) which in turn increases the velocity. The ongoing analysis explains why different polymer-filled metal filaments manufacturers specify different printing speeds for the same metal (or alloy) with different particle loading.

Fig. 12b shows the shear viscosity response of different powder contents with feeding rates. The figure indicates that at the capillary outlet the shear viscosity increases as the feeding rate increases due to an increase in the shear rates. Also, the shear viscosity increases as the powder contents increase. A comparison of the four powder contents responses with feeding rates from the figure reveals that for powder content below 140 mm/min, the shear viscosity curve is almost the same for 45, 50, and 56 vol% and exhibited an almost horizontal profile before turning upwards. However, the 60 vol% diverges upwards from the other three and increases monotonically for all simulated feeding rates.

This indicates that the EMP feedstock green part extrudate shape dimensional stability is expected to increase when the formulated binder is impregnated with high powder contents above 56 vol%, which confirms the reason why the printing trials demonstrated with this binder was done at powder content of 59 vol% as reported in [31,32]. However, in their work [31,32], they performed the shaping (printing) of the green parts without the use of thermal-fluid simulation after several real trials to determine printing parameters. However, the current study underscores the usefulness of computational simulation in selecting process parameters for polymer-filled metal filaments with different particle loading for material extrusion additive manufacturing.

3.4. Influence of powder contents on the flow through hot-end

In this section, different powder contents were investigated and the printer temperature in this simulation was set to 503 K within the feeding rates of 40, 120, 180, 240, and 280 mm/min. The powder contents considered correspond to those simulated in the previous section. The target predicted variables in this simulation are the core temperature which represents the lowest temperature predicted at the outlet of the capillary exit of the hot-end and the shear viscosity at the exit. The core temperature corresponds to the central temperature at the capillary exit and is used to also quantify the effectiveness of heat transfer from the wall to the central axis. Also, the shear viscosity provides information about the possible dimensional stability and shape retention of the extrudate during deposition.

The core temperature as a function of powder content under different feeding rates is presented in Fig. 13a. The core temperature decreases as the feeding rates increase; however, the temperature equilibrates the liquefier temperature at the lowest feeding rate of 40 mm/min for all powder contents explored. Additionally, the temperature increases as the powder contents in the binder system increases.

From 180 to 280 mm/min feeding rates, the temperature is the same at the lowest powder content of 45 vol%. As the powder contents increase and at 180 mm/min feeding rates the temperature increases rapidly away from the 240 and 280 mm/min feeding rates. Within the powder contents of 45 to 50 vol%, the core temperature for the 240 and 280 mm/min feeding rates are the same, but as the feeding rates increase the lower of the two feeding rates diverges upwards towards higher temperature values. Similar relationships were observed in Fig. 12b for the shear viscosity as a function of powder contents and feeding rates. However, at lower feeding rates (40 and 120 mm/min), the viscosity is lowest for all powder contents explored with the shear viscosities increasing and merging towards the highest powder contents. The increase in the viscosity for all the feeding rates considered is evident from the figure since the solid loading in the binder system has been reported to increase the viscosity of highly-filled polymers [14,44–47]. Some obvious reported advantages of high particle loading for metal-filled filaments are an increase in the sintered density, high dimensional stability of the printed green parts, slumping, and low shrinkage, the opposite is the case for low parting loading. In as much as high particle

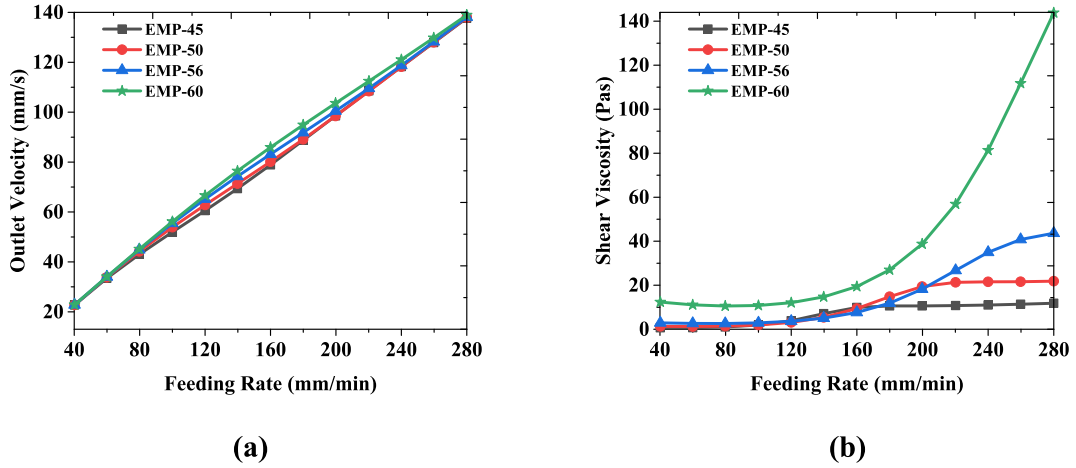

Fig. 12. (a) Average outlet velocity and (b) average shear viscosity at the nozzle exit as a function of feeding rates for different metal powder content. Simulation condition: liquefier temperature of 503 K, nozzle diameter of 0.6 mm, and barrel diameter of 3.2 mm.

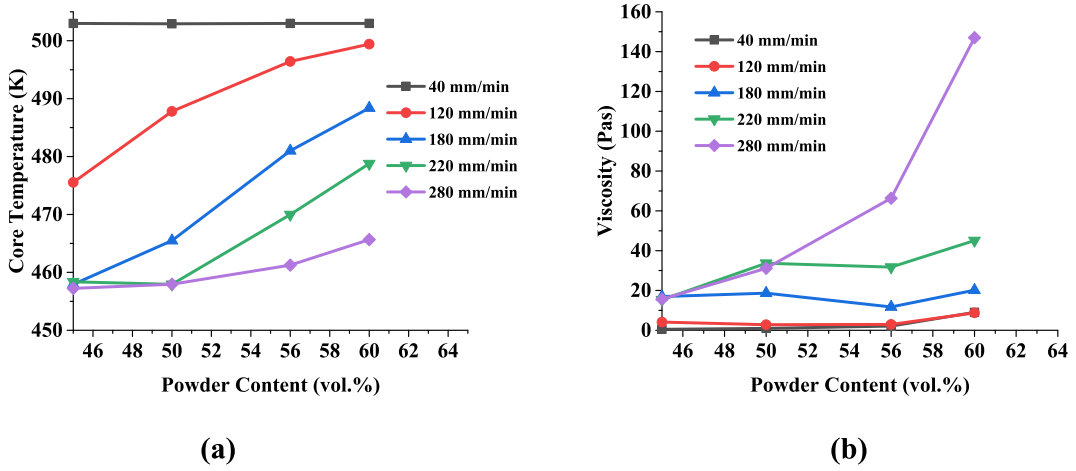

Fig. 13. (a) Core temperature and (b) average shear viscosity at the nozzle exit as a function of feeding rates for different metal powder content. Simulation condition: printer set temperature of 503 K, nozzle diameter of 0.6 mm.

loading is desired, however, excessive-high particle loading poses extrusion challenges such as brittleness of the filament leading to breakage and extrusion failure due to high viscosity. Some manufacturers such as the Virtual Foundry have recommended the use of filawarmer to preheat the filaments to 60 °C to lower the brittleness of the filament before feeding it into the filament to avoid extrusion failure. The reported viscosities (See Fig. 7b) of the filament as the feeding rates increase at the nozzle exit for the Virtual Foundry filaments are very high and may cause extrusion failure if printed without the use of filawarmer.

3.5. Comparison of the simulation results of the present model for EMP feedstock with maximum filament failure force

In this section, the extrusion force which represents the pressure force provided by the extruder from the upstream rigid solid portion of the filament to push the extrudate out of the nozzle orifice is predicted and compared with the maximum force the filament can sustain without failure. The maximum force that a filament can sustain before failure was experimentally determined by Singh et al. [12] by creating significant surface indentations on the surface of the filament at a feeding rate of 30 to 960 mm/min. They [12] determined the three-dimensional optical microscope imaging of the shear contact area using the method suggested by Go et al. [29]. Then, the shear strength of the filament was determined from the ultimate tensile strength of the filament using stress-strain measured data. Having the shear strength multiplied by the shear contact area gives the maximum force the filament can sustain without failure. They used 59 vol% of Ti-6Al-4V particles to compound different PMF made from different binders and different particle sizes (coarse and fine). The filament used is 1.75 mm in diameter and the diameter of the hot-end exit nozzle is 0.4 mm. It was reported that the maximum force three of the filaments can sustain before failure was approximately 1 N [12].

In the present study, 59 vol% of Ti-6Al-4V EMP feedstock was simulated to compare the performance of the numerical model. The thermophysical properties of the EMP used for the simulation were predicted using the procedure described previously for 45, 50, 56, and 60 EMP feedstocks. It should be noted that the choice of using this data for comparison was motivated by the fact that it was the same group of researchers that developed the binder system used to estimate the thermophysical properties of the EMP feedstocks simulated.

Fig. 14 presents the predicted extrusion force against feeding rates for 59 vol% of Ti-6Al-4V filaments for 0.4 and 0.6 mm nozzle sizes and 2 mm barrel diameter. The walls of the conical and capillary sections were set to a printer temperature of 503 K, and the heat transfer coefficients were determined using the procedure discussed in the previous sections. The simulation was performed from feeding rates of 40 to 600 mm/min. The figure shows that the extrusion force increases as the feeding rates

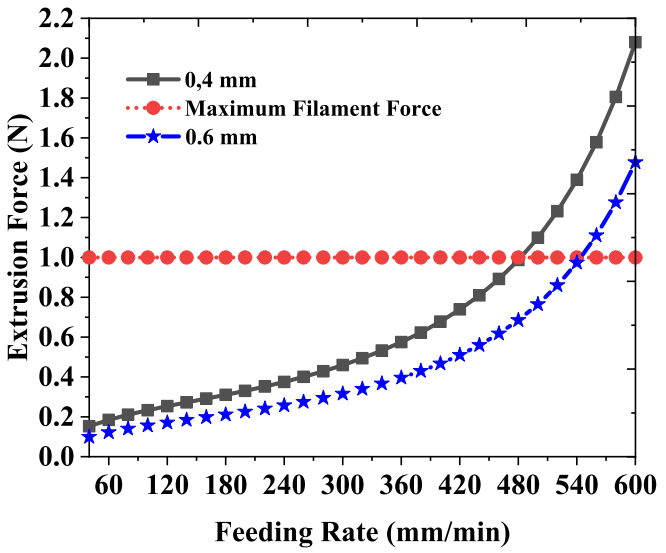

Fig. 14. Predicted extrusion force as a function of feeding rates for 0.4 and 0.6 mm nozzle diameters, and 2 mm barrel diameter at a printer temperature of 503 K.

increase in a linear pattern up to feeding rates of 400 and 480 mm/min for 0.4 mm and 0.6 mm nozzle diameter, above these values, the extrusion force increases exponentially and crosses the maximum filament force (red dotted broken line). The transition from linear to exponential for extrusion force followed the generally reported trends in literature for measured and numerically estimated unfilled filament force data [16,17,20,21,26,29]. The maximum force of 1 N was reached at feeding rates of 480 and 540 mm/min for the 0.4 and 0.6 mm, respectively.

The estimated feeding rates may be taken as the maximum permissible feeding rates. This means that the filament can be extruded below the maximum permissible feeding rates without extrusion failure or filament breakage. Also, the 0.6 mm nozzle diameter would be printed at a higher printing speed than the 0.4 mm.

The maximum extrusion forces predicted for 0.4 and 0.6 mm at the highest feeding rates explored are 2 and 1.5 N, respectively. The reason for the higher extrusion force and lower feeding rates transition from linear to exponential force increase for the 0.4 mm nozzle is that the feedstocks experience higher pressure drops, shear viscosity, and shear rates at the orifice than the bigger one during material extrusion of PMF. Additionally, analytical relations showed that pressure drop is inversely proportional to the capillary orifice diameter and directly proportional to viscosity for a non-Newtonian fluid [37]. Therefore, the smaller the nozzle diameter the higher the pressure drop with a corresponding increase in the pressure force (extrusion force) and vice versa.

Comparing the predicted extrusion forces with the maximum failure force the filament can sustain before failure, it can be easily seen that the CFD results provide values that are less than or equal to 1 N over a wide range of feeding rates explored. The analytically estimated maximum permissible feeding rates for 0.4 mm nozzle diameter that corresponds to a maximum force of 1 N assuming isothermal condition by Singh et al. [12] for fine and coarse powder are 150 mm/min and 456 mm/min, respectively. These values when compared to the current CFD predicted maximum permissible feeding rates are lower. Though the current work did not study the effect of particle sizes on the extrusion forces, however, one point that was reported in the literature is that analytical models underpredict the measured extrusion force due to oversimplification of the model and some other assumptions including the assumption of isothermal [20,26]. It is of interest to note that the analytical solution never considered the shear rate-temperature dependability of viscosity of the feedstocks and complex heat transfer mechanisms during processing which may have affected the estimated result of Singh et al. [12], thus lacking the general trend of extrusion force-feeding rates relationship described previously.

4. Conclusions

In this work, a Titanium 64-5 filament was obtained from industry and its thermophysical properties were experimentally measured and labeled EXP feedstock. Another Titanium 64-5 filament thermophysical properties was empirically estimated using the binder material property published documented data and was labeled EMP feedstock. The measured thermophysical properties of the industrially formulated filament were compared to empirically estimated thermophysical properties of another Titanium 64-5 filament. Then, a thermal-fluid model was used to simulate the temperature, shear rates, velocity, viscosity, and extrusion force, and useful results and conclusions were discovered as follows.

1. Some experimentally measured and empirically predicted thermophysical properties of the two types of filaments such as density and thermal conductivity values are very similar.
2. Given the same powder loading of 44.5 vol%, the responses of the two filaments quantified in terms of shear rate, and temperature with feeding rates are almost the same at a certain range of extrusion regimes. However, in all the feeding rates simulated the predicted viscosity for EXP feedstock is much greater than that of EMP feedstock.
3. At the central axis in the conical section where y = 2.4 mm, the predicted temperature for EXP is 461 K which is higher than the temperature for EMP which is 446 K, and it depicts a temperature difference of 15 K. While at the nozzle outlet, the temperature for EXP is 428 K which is higher than that of EMP (400 K) with a temperature difference of 28 K.
4. The comparison of the shear viscosity for both feedstocks, shows that the EMP feedstocks may present successive layer-by-layer shape deposition stability difficulties of the green parts since it shows an excessively lower viscosity at all feeding rates investigated.
5. The exit temperature decreases with feeding rates, increases with a decrease in the Gz, and increases with the powder contents and vice versa.
6. The results show that extrusion force increases as the feeding rates increase in a linear pattern up to feeding rates of 400 and 480 mm/min for 0.4 mm and 0.6 mm nozzle diameter, above these values, the extrusion force increases exponentially and crosses the maximum filament force (red dotted broken line).

CRediT authorship contribution statement

Gaius Chukwuka Nzebuka: Writing – review & editing, Writing – original draft, Visualization, Validation, Supervision, Software, Resources, Methodology, Investigation, Formal analysis, Data curation, Conceptualization. **Chukwuzubelu Okenwa Ufodike:** Writing – review & editing, Writing – original draft, Visualization, Supervision, Software, Resources, Project administration, Methodology, Investigation, Formal analysis, Data curation, Conceptualization. **Al Mazedur Rahman:** Writing – review & editing, Methodology, Investigation. **Matthew B. Minus:** Writing – review & editing, Investigation. **Chijioke Peter Egole:** Writing – review & editing.

Declaration of competing interest

There is no conflict of interest.

Acknowledgments

We thank Tricia Suess and Bradley D. Woods of The Virtual Foundry

(TVF) for providing the Titanium 64-5 filament used for this work. We thank Professor Ufodike Research Group (PURG), and the Digital Manufacturing & Distribution Lab (DMD-Lab) at Texas A&M Engineering Experiment Station, Texas A&M University, College Station, TX.

References

[1] Javaid M, Haleem A. Additive manufacturing applications in medical cases: a literature based review. Alexandria Journal of Medicine 2018;54(4):411–22.
[2] Nurhudan AI, Supriadi S, Whulanza Y, Saragih AS. Additive manufacturing of metallic based on extrusion process: a review. Journal of Manufacturing Processes 2021;66:228–37.
[3] Rosli N, Alkahari M, Ramli F, Maidin S, Sudin M, Subramoniam S, et al. Design and development of a low-cost 3D metal printer. Journal of Mechanical Engineering Research & Developments (JMERD) 2018;41(3):47–54.
[4] Chen L, Huang J, Lin C, Pan C, Chen S, Yang T, et al. Anisotropic response of Ti-6Al-4V alloy fabricated by 3D printing selective laser melting. Mater Sci Eng A 2017;682:389–95.
[5] Chern AH, Nandwana P, McDaniels R, Dehoff RR, Liaw PK, Tryon R, et al. Build orientation, surface roughness, and scan path influence on the microstructure, mechanical properties, and flexural fatigue behavior of Ti–6Al–4V fabricated by electron beam melting. Mater Sci Eng A 2020;772:138740.
[6] Kok Y, Tan XP, Wang P, Nai M, Loh NH, Liu E, et al. Anisotropy and heterogeneity of microstructure and mechanical properties in metal additive manufacturing: a critical review. Materials & Design 2018;139:565–86.
[7] Zhang Y, Bai S, Riede M, Garratt E, Roch A. A comprehensive study on fused filament fabrication of Ti-6Al-4V structures. Addit Manuf 2020;34:101256.
[8] Gonzalez-Gutierrez J, Cano S, Schuschnigg S, Kukla C, Sapkota J, Holzer C. Additive manufacturing of metallic and ceramic components by the material extrusion of highly-filled polymers: a review and future perspectives. Materials 2018;11(5):840.
[9] Gonzalez-Gutierrez J, Godec D, Guráň R, Spoerk M, Kukla C, Holzer C. 3D printing conditions determination for feedstock used in fused filament fabrication (FFF) of 17-4PH stainless steel parts. Metalurgija 2018;57(1–2):117–20.
[10] Gonzalez-Gutierrez J, Duretek I, Arbeiter F, Kukla C, Holzer C. Filler content and properties of highly filled filaments for fused filament fabrication of magnets. SPE ANTEC 2017;2017.
[11] Gonzalez-Gutierrez J, Duretek I, Kukla C, Poljšak A, Bek M, Emri I, et al. Models to predict the viscosity of metal injection molding feedstock materials as function of their formulation. Metals 2016;6(6):129.
[12] Singh P, Balla VK, Tofangchi A, Atre SV, Kate KH. Printability studies of Ti-6Al-4V by metal fused filament fabrication (MF3). Int J Refract Met Hard Mater 2020;91:105249.
[13] Liu B, Wang Y, Lin Z, Zhang T. Creating metal parts by fused deposition modeling and sintering. Mater Lett 2020;263:127252.
[14] Wagner MA, Hadian A, Sebastian T, Clemens F, Schweizer T, Rodriguez-Arbaizar M, et al. Fused filament fabrication of stainless steel structures-from binder development to sintered properties. Addit Manuf 2022;49:102472.
[15] Ufodike CO, Nzebuka GC, Egole CP. Prediction of limiting casting speed in a horizontal direct-chill casting through numerical modeling and simulation. Metals 2023;13(6):1071.
[16] Kattinger J, Ebinger T, Kurz R, Bonten C. Numerical simulation of the complex flow during material extrusion in fused filament fabrication. Addit Manuf 2022;49:102476.
[17] Nzebuka GC, Ufodike CO, Rahman AM, Gwynn CM, Ahmed MF. Numerical modeling of the effect of nozzle diameter and heat flux on the polymer flow in fused filament fabrication. Journal of Manufacturing Processes 2022;82:585–600.
[18] Phan DD, Horner JS, Swain ZR, Beris AN, Mackay ME. Computational fluid dynamics simulation of the melting process in the fused filament fabrication additive manufacturing technique. Addit Manuf 2020;33:101161.
[19] Pigeonneau F, Xu D, Vincent M, Agassant J-F. Heating and flow computations of an amorphous polymer in the liquefier of a material extrusion 3D printer. Addit Manuf 2020;32:101001.
[20] Serdeczny MP, Comminal R, Mollah MT, Pedersen DB, Spangenberg J. Numerical modeling of the polymer flow through the hot-end in filament-based material extrusion additive manufacturing. Addit Manuf 2020;36:101454.
[21] Ufodike CO, Nzebuka GC. Investigation of thermal evolution and fluid flow in the hot-end of a material extrusion 3D Printer using melting model. Addit Manuf 2022;49:102502.
[22] Colon AR, Kazmer DO, Peterson AM. The dependency chain in material extrusion additive manufacturing: shaft torque, infeed load, melt pressure, and melt temperature. Addit Manuf 2023;77:103780.
[23] Zhang J, Meng F, Ferraris E. Temperature gradient at the nozzle outlet in material extrusion additive manufacturing with thermoplastic filament. Addit Manuf 2023;73:103660.
[24] Ufodike CO, Nzebuka GC, Rahman AM. Combine effect of feeding rate and modeling parameter on the extrusion pressure in material extrusion additive manufacturing. Manufacturing Letters 2023;35:485–92.
[25] Hopmann C, Michaeli W. Extrusion dies for plastics and rubber: design and engineering computations. Carl Hanser Verlag GmbH Co KG; 2016.
[26] Serdeczny MP, Comminal R, Pedersen DB, Spangenberg J. Experimental and analytical study of the polymer melt flow through the hot-end in material extrusion additive manufacturing. Addit Manuf 2020;32:100997.
[27] Agarwala MK, Jamalabad VR, Langrana NA, Safari A, Whalen PJ, Danforth SC. Structural quality of parts processed by fused deposition. Rapid Prototyp J 1996;2(4):4–19.
[28] Incropera F, DeWitt D. Fundamentals of heat transfer 1wiley. New York 1990;19852:8.
[29] Go J, Schiffres SN, Stevens AG, Hart AJ. Rate limits of additive manufacturing by fused filament fabrication and guidelines for high-throughput system design. Addit Manuf 2017;16:1–11.
[30] Kate KH, Enneti RK, Onbattuvelli VP, Atre SV. Feedstock properties and injection molding simulations of bimodal mixtures of nanoscale and microscale aluminum nitride. Ceram Int 2013;39(6):6887–97.
[31] Singh P, Shaikh Q, Balla VK, Atre SV, Kate KH. Estimating powder-polymer material properties used in design for metal fused filament fabrication (DfMF3). Jom 2020;72(1):485–95.
[32] Shaikh MQ, Singh P, Kate KH, Freese M, Atre SV. Finite element-based simulation of metal fused filament fabrication process: distortion prediction and experimental verification. Journal of Materials Engineering and Performance 2021;30:5135–49.
[33] Kate KH, Onbattuvelli VP, Enneti RK, Lee SW, Park S-J, Atre SV. Measurements of powder–polymer mixture properties and their use in powder injection molding simulations for aluminum nitride. Jom 2012;64:1048–58.
[34] Mills KC. Recommended values of thermophysical properties for selected commercial alloys. Woodhead Publishing; 2002.
[35] Nor NM, Muhamad N, Ibrahim M, Ruzi M, Jamaludin K. Optimization of injection molding parameter of Ti-6Al-4V powder mix with palm stearin and polyethylene for the highest green strength by using Taguchi method. International Journal of Mechanical and Materials Engineering 2011;6(1):126–32.
[36] Tanner RI. Engineering rheology. OUP Oxford; 2000.
[37] Barnes HA, Hutton JF, Walters K. An introduction to rheology. Elsevier; 1989.
[38] Bird R, Armstrong R, Hassager O. Dynamics of polymeric liquids. New York: John Wiley & Sons; 1987.
[39] Rueda MM, Auscher M-C, Fulchiron R, Périé T, Martin G, Sonntag P, et al. Rheology and applications of highly filled polymers: a review of current understanding. Prog Polym Sci 2017;66:22–53.
[40] Kalyon DM, Dalwadi D, Erol M, Birinci E, Tsenoglu C. Rheological behavior of concentrated suspensions as affected by the dynamics of the mixing process. Rheologica Acta 2006;45:641–58.
[41] Gulmus SA, Yilmazer U. Effect of volume fraction and particle size on wall slip in flow of polymeric suspensions. J Appl Polym Sci 2005;98(1):439–48.
[42] Suwardie H, Yazici R, Kalyon D, Kovenklioglu S. Capillary flow behaviour of microcrystalline wax and silicon carbide suspension. J Mater Sci 1998;33:5059–67.
[43] ANSYS Polyflow 22. Canonsburg, PA, USA: ANSYS, Inc; 2011.
[44] Agarwala M, Weeren RV, Bandyopadhyay A, Safari A, Danforth S, Priedeman W. Filament feed materials for fused deposition processing of ceramics and metals. In: 1996 International solid freeform fabrication symposium; 1996.
[45] Agarwala M, Weeren RV, Bandyopadhyay A, Whalen P, Safari A, Danforth S. Fused deposition of ceramics and metals: an overview. In: 1996 international solid freeform fabrication symposium; 1996.
[46] Kukla C, Gonzalez-Gutierrez J, Cano SC, Burkhardt C, Hampel S, Moritz T, et al. Fused filament fabrication for the production of metal and/or ceramic parts and feedstocks therefore. In: 19th Plansee seminar. Plansee AG; 2017.
[47] Kukla C, Gonzalez-Gutierrez J, Cano SC, Hampel S, Burkhardt C, Moritz T, et al. Fused filament fabrication (FFF) of PIM feedstocks. Congreso Iberoamericano de Pulvimetalurgia; 2017. p. 1–6.